

Superconductivity in trilayer nickelate $\text{La}_4\text{Ni}_3\text{O}_{10}$ under pressure

Mingxin Zhang^{1#}, Cuiying Pei^{1#}, Xian Du^{2#}, Weixiong Hu^{1#}, Yantao Cao^{3,4#}, Qi Wang^{1,5}, Juefei Wu¹, Yidian Li², Huanyu Liu¹, Chenhaoping Wen¹, Yi Zhao¹, Changhua Li¹, Weizheng Cao¹, Shihao Zhu¹, Qing Zhang^{1,6}, Na Yu¹, Peihong Cheng¹, Lili Zhang⁷, Zhiwei Li³, Jinkui Zhao⁴, Yulin Chen^{1,5,8}, Hanjie Guo^{4*}, Congjun Wu^{9,10}, Fan Yang^{11*}, Shichao Yan^{1,5*}, Lexian Yang^{2*}, Yanpeng Qi^{1,5,6*}

1. School of Physical Science and Technology, ShanghaiTech University, Shanghai 201210, China

2. State Key Laboratory of Low Dimensional Quantum Physics, Department of Physics, Tsinghua University, Beijing 100084, China

3. Key Lab for Magnetism and Magnetic Materials of the Ministry of Education, School of Physical Science and Technology, Lanzhou University, Lanzhou 730000, Gansu, China

4. Songshan Lake Materials Laboratory, Dongguan 523808, Guangdong, China

5. ShanghaiTech Laboratory for Topological Physics, ShanghaiTech University, Shanghai 201210, China

6. Shanghai Key Laboratory of High-resolution Electron Microscopy, ShanghaiTech University, Shanghai 201210, China

7. Shanghai Synchrotron Radiation Facility, Shanghai Advanced Research Institute, Chinese Academy of Sciences, Shanghai 201203, China

8. Department of Physics, Clarendon Laboratory, University of Oxford, Parks Road, Oxford OX1 3PU, UK

9. Institute for Theoretical Sciences, Westlake University, Hangzhou 310024, Zhejiang, China

10. New Cornerstone Science Laboratory, Department of Physics, School of Science, Westlake University, Hangzhou 310024, Zhejiang, China

11. School of Physics, Beijing Institute of Technology, Beijing 100081, China

These authors contribute equally to this work.

* Correspondence should be addressed to Y.P.Q. (qiyp@shanghaitech.edu.cn) or L.X.Y. (lxyang@tsinghua.edu.cn) or S.C.Y. (yanshch@shanghaitech.edu.cn) or F.Y. (yangfan_blg@bit.edu.cn) or H.J.G. (hjguo@sslslab.org.cn)

ABSTRACT

Nickelate superconductors have attracted a great deal of attention over the past few decades due to their similar crystal and electronic structures with high-temperature cuprate superconductors. Here, we report the superconductivity in a pressurized Ruddlesden-Popper phase single crystal, $\text{La}_4\text{Ni}_3\text{O}_{10}$ ($n = 3$), and its interplay with the density wave order in the phase diagram. With increasing pressure, the density wave order as indicated by the anomaly in the resistivity is progressively suppressed, followed by the emergence of the superconductivity around 25 K. Our angle-resolved photoemission spectroscopy measurements reveal that the electronic structure of $\text{La}_4\text{Ni}_3\text{O}_{10}$ is very similar to that of $\text{La}_3\text{Ni}_2\text{O}_7$, suggesting unified electronic properties of nickelates in Ruddlesden-Popper phases. Moreover, theoretical analysis unveils that antiferromagnetic (AFM) super-exchange interactions can serve as the effective pairing interaction for the emergence of superconductivity (SC) in pressurized $\text{La}_4\text{Ni}_3\text{O}_{10}$. Our research provides a new platform for the investigation of the unconventional superconductivity mechanism in Ruddlesden-Popper trilayer perovskite nickelates.

Introduction

The discovery of superconductivity in cuprates has opened the avenue to explore high-temperature (high- T_c) superconductivity^{1, 2}. Almost all the discovered cuprates superconductors so far share a common two-dimensional CuO_2 plane and half-filled Cu $3d^9$ electronic configuration, which are believed to be essential to the emergence of high- T_c superconductivity^{3, 4}. Besides cuprates, iron-based superconductors are another prime material family with superconductivity well above the McMillan limit at ambient pressure^{5, 6}. In contrast to the cuprates, iron-based superconductors with Fe $3d^6$ electronic configuration have a multi-band and multi-orbital nature^{7, 8}. Despite sustained efforts that have been devoted more than three decades, the full understanding of their superconductivity mechanism remains a challenging and long-sought problem in condensed matter physics.

Nickelates are considered to be an ideal candidate for exploring new cuprate-like high- T_c superconductivity due to the proximity of $\text{Ni}^+(3d^9)$ electron configuration⁹. However, superconductivity was not experimentally realized in nickelates until 2019, when *Li et al.* discovered superconductivity within the thin films of infinite-layer nickelates $\text{Nd}_{1-x}\text{Sr}_x\text{NiO}_2$ with $T_c \sim 9\text{--}15\text{ K}$ ^{10, 11}, which quickly promoted renewed interest in the exploration of nickel-based superconductors. Subsequently, T_c has been extended to other infinite-layer nickelates with different rare-earth elements^{12, 13, 14, 15}. However, superconductivity is limited to thin film materials. Structurally, whether there exists a nickelate superconductor family with bulk superconductivity is still an open question.

Recently, the experimental breakthrough revealed high- T_c superconductivity above liquid-nitrogen temperature in pressurized bulk $\text{La}_3\text{Ni}_2\text{O}_7$ single crystals, which is one of the Ruddlesden-Popper (RP) phases $\text{La}_{n+1}\text{Ni}_n\text{O}_{3n+1}$ ($n = 2$) with the valence of $\text{Ni}^{2.5+}$ ¹⁶. The synchrotron X-ray diffraction (XRD) patterns and Density functional theory (DFT) calculations indicate that the $\text{La}_3\text{Ni}_2\text{O}_7$ undergoes a structural phase transition from *Amam* to *I4/mmm* with the emergence of superconductivity, and a series of follow-up experiments have elaborated that oxygen defects and hydrostatic environment are essential for the discovery of superconductivity^{17, 18, 19, 20, 21, 22, 23}. Moreover, many theoretical works are put forward to understand the underlying mechanisms of high- T_c superconductivity in $\text{La}_3\text{Ni}_2\text{O}_7$ ^{24, 25, 26, 27, 28, 29, 30, 31, 32, 33, 34, 35, 36, 37, 38, 39}.

Among RP phase nickelates, the trilayer $\text{La}_4\text{Ni}_3\text{O}_{10}$ ($n = 3$) has drawn more attention due to the metallic ground state and metal-to-metal transition at intermediate temperatures^{40, 41, 42, 43}. The nominal valence state of Ni is +2.65 in $\text{La}_4\text{Ni}_3\text{O}_{10}$, which is usually believed to be given by mixed valence states of Ni^{2+} ($3d^8$) and Ni^{3+} ($3d^9$). Considering the similar crystal structure and Ni valence with $\text{La}_3\text{Ni}_2\text{O}_7$, it is natural to consider investigating the superconductivity and electronic structure in pressurized $\text{La}_4\text{Ni}_3\text{O}_{10}$ single crystals.

In this work, we grow high-quality $\text{La}_4\text{Ni}_3\text{O}_{10}$ single crystal with an optical-image floating zone furnace under high oxygen pressure and perform high-pressure transport measurements using NaCl as the pressure-transmitting medium to improve the hydrostatic environment. We find superconductivity with a T_c of 25 K in $\text{La}_4\text{Ni}_3\text{O}_{10}$ single crystals at around 60 GPa. By combining scanning tunneling microscopy/spectroscopy, angle-resolved photoemission spectroscopy, and *ab initio* calculation, we systematically investigate the electronic structure of trilayer nickelate $\text{La}_4\text{Ni}_3\text{O}_{10}$. These observations broaden and contribute to the superconducting family of nickelates.

Results and discussion

Trilayer nickelate. $\text{La}_4\text{Ni}_3\text{O}_{10}$, one of the RP phases $\text{La}_{n+1}\text{Ni}_n\text{O}_{3n+1}$ ($n = 3$) nickelates, crystallizes in a monoclinic structure ($a = 5.41$ Å, $b = 5.47$ Å, $c = 14.22$ Å), consisting of 3 layers of perovskite-type LaNiO_3 , separated by a single rocksalt-type LaO layer along the crystallographic c -axis direction (Fig. 1a). As shown in Fig. 1b, high-angle annular dark-field (left) and annular bright-field (right) transmission electron microscopy images (Fig. 1b) illustrates each unit contains well-ordered three layers of inclined NiO_6 octahedral layers stacking along the c -axis direction. The inclination of the NiO_6 octahedra leads to the bucking of the Ni-O planes. The side-view crystal structure of the La-Ni-O layer in the monoclinic phase of $\text{La}_4\text{Ni}_3\text{O}_{10}$ is shown in Fig. 1c. As we can see, the Ni-O bonds are tilted in the bc plane instead of the ac plane, resulting in a unidirectional structural reconstruction compared to that of the tetragonal phase. Figure 1d shows the in-plane unit cells for the tetragonal and the monoclinic phases. The size of the reconstructed monoclinic unit cell is twice that of the tetragonal unit cell due to the structural reconstruction. The unidirectional reconstruction results in a stripe-like structure as illustrated by the light blue ribbons in Fig. 1d. The periodicity of the stripe is $\sqrt{2}$ times of the tetragonal lattice a_{tet} , as indicated by the $Q_{\sqrt{2}}$ in the Fourier transform (FT) of the NiO lattice (Fig. 1e).

The unidirectional reconstruction in $\text{La}_4\text{Ni}_3\text{O}_{10}$ can be confirmed by the low-temperature scanning tunneling microscopy (STM) measurements. Figure 1f shows a typical STM topography taken on the large-area LaO-terminated surface. On the LaO surface, we observe an ordered square lattice with some adatom-like impurities and several rip-like dark stripes along the diagonal direction of the square lattice. These features can be seen more clearly in the zoom-in STM topography as shown in Fig. 1g. The square lattice is measured to be 0.40 nm, which is consistent with the in-plane LaO tetragonal lattice as shown in Fig. 1d. This indicates that the rip-like dark stripes are along the reconstruction direction. To further quantify the reconstructed surface, we perform FT to the STM topography (Fig. 1h). In the FT image, apart from the Q_{tet} originated from LaO in-plane tetragonal lattice, there is a set of unidirectional Q_1 vector, which is $1/\sqrt{2}$ times of the Q_{tet} . The length and direction of the Q_1 wave vector are the same as the $Q_{\nu 2}$ in Fig. 1e, indicating that there exists a stripe-like unidirectional structural reconstruction on the LaO surface. Interestingly, the rip-like dark stripes in the real space are also along the reconstructed stripe direction (Fig. 1g), which suggests that the rip-like dark stripes might be related to the reconstruction in $\text{La}_4\text{Ni}_3\text{O}_{10}$ due to the unidirectional strain-like effect.

Transport and electronic properties under ambient pressure. Figures 2a-c show the resistivity, magnetic susceptibility, and heat capacity measured on $\text{La}_4\text{Ni}_3\text{O}_{10}$ single crystals. The resistivity decreases with cooling temperature from 300 K, revealing typical metallic behavior. A pronounced anomalous peak at around 130 K, suggests possible density-wave states. The in-plane magnetic susceptibility was measured under a magnetic field of 0.4 T, which shows a sharp decrease at the $T^* \sim 132$ K, similar to typical charge or spin density wave materials such as $\text{K}_{0.3}\text{MoO}_3$ ⁴⁴, CsV_3Sb_5 ⁴⁵, LaFeAsO_5 ⁵. The temperature-dependent heat capacity also exhibits an anomalous peak at the same temperature, and it can be well fitted by the formula $C_p/T = \gamma + \beta T^2$, where γ is the Sommerfeld coefficient. The fit yields $\gamma = 13.5 \text{ mJ mole}^{-1}\text{K}^{-2}$ and $\beta = 0.34 \text{ mJ mole}^{-1} \text{K}^{-4}$, which agrees with the previous measurement⁴¹. The Debye temperatures

and density of states $N(E_F)$ can be estimated as 459 K and 2.1 states eV^{-1} per Ni, respectively.

Furthermore, we investigate the electronic structure of $\text{La}_4\text{Ni}_3\text{O}_{10}$ using high-resolution angle-resolved photoemission spectroscopy (ARPES). Figs. 2d and 2e show the constant energy contours at the Fermi level (E_F) and -0.1 eV. Consistent with a previous report⁴⁶, the Fermi surface is mainly made up of a nearly circular electron pocket around the $\bar{\Gamma}$ point and large square-like hole pockets centered at the $\bar{\Gamma}$ point. Figs. 2f and 2g show the band dispersions along the $\bar{\Gamma}\bar{X}$ and $\bar{\Gamma}\bar{M}$ directions, respectively. While there are clear dispersive bands near the E_F , waterfall-like structures appear at higher binding energies. Overall, the experimental band structure of $\text{La}_4\text{Ni}_3\text{O}_{10}$ is very similar to that of $\text{La}_3\text{Ni}_2\text{O}_7$ ³⁰, despite their different crystal structure. The *ab initio* calculated constant energy contours at selected energies and band structure along high-symmetry paths are presented in Figs. 2h-j. Due to the trilayer structure of Ni-O octahedron slabs in the crystal structure, there are 3 sets of bands in the low-energy Ni-O based band structure. Both the $3d_{x^2-y^2}$ and $3d_{z^2}$ -dominated bands split into bonding, non-bonding, and anti-bonding bands. In particular, both the bonding and non-bonding bands of $3d_{z^2}$ -dominated bands cross E_F , in contrast to the situation in $\text{La}_3\text{Ni}_2\text{O}_7$ ¹⁶. However, only one set of energy bands is observed in the ARPES experiments, which remains a mystery⁴⁶.

Superconductivity in pressurized single crystal. The resistivity anomaly indicates that $\text{La}_4\text{Ni}_3\text{O}_{10}$ is located in the vicinity of an electronic instability. It is well known that superconductivity often appears near the critical point of structural or density waves. In this respect, pressure has been proven to be a convenient and effective way to modify lattice parameters and systematically influence the corresponding electronic states without introducing other factors. Motivated by these advantages, we measured the electrical resistance of $\text{La}_4\text{Ni}_3\text{O}_{10}$ single crystals at various pressures. Figure 3a shows the typical resistance curves of $\text{La}_4\text{Ni}_3\text{O}_{10}$ for pressure up to 60 GPa. The resistance anomaly is sensitive to external pressures. With increasing pressure to 2.3 GPa, the temperature of the resistance anomaly shifts to ~ 120 K. As the pressure continues to

increase to 14.0 GPa, the anomalous feature in the resistance curve becomes broadened and less pronounced. At 23.1 GPa, the resistance anomaly is suppressed further and the resistance curve displays a slight upturn at the lower temperatures followed by a down-turn feature. When the pressure approaches 32.3 GPa, the temperature dependence of resistance changes to that of a normal metal. Interestingly, a distinct behavior characterized by a resistance drop of about 8.5 K emerges and this behavior becomes more pronounced as the pressure is increased, indicating the superconducting transition. The superconducting T_c continuously increases and reaches 23.5 K at 56.8 GPa. Especially, with the appearance of superconductivity, T -linear resistance becomes clear gradually in the normal state (Fig. 3b). It is worth noting that the resistance drops by 95% from the normal state to the lowest temperature, which suggests a superconducting transition. Compared with Run 1, the resistance anomaly peak was suppressed below 10 GPa in Run 2 (Fig. S4), followed by the emergency of sharp drops. The superconducting T_c reaches 25 K at approximately 42.5 GPa. Presently, small residue resistance was observed, likely due to the less hydrostatic conditions in the diamond anvil cell (DAC).

To further determine whether the observed resistance drop is truly associated with a superconducting transition, we performed resistance measurements under various magnetic fields. As displayed in Fig. S5, the resistance drop of $\text{La}_4\text{Ni}_3\text{O}_{10}$ is progressively suppressed to lower temperatures, which implies a superconducting transition. The onset of superconductivity seems insensitive to the external magnetic fields and the transition width becomes broad with increasing magnetic field, which is similar to high- T_c cuprates. Superconductivity survives even under magnetic field $\mu_0 H = 9$ T. As shown in the inset of Fig. 3b, the upper critical field $\mu_0 H_{c2}$ can be well-fitted using the empirical Ginzburg-Landau formula $\mu_0 H_{c2}(T) = \mu_0 H_{c2}(T) (1 - t^2)/(1 + t^2)$, where $t = T/T_c$. The superconducting transition is robust and extrapolated upper critical field $\mu_0 H_{c2}(0)$ of $\text{La}_4\text{Ni}_3\text{O}_{10}$ can reach 31.1 T at 67.7 GPa in Run 3, which yields a Ginzburg-Landau coherence length $\xi_{\text{GL}}(0)$ of 3.25 nm.

Several independent high-pressure transport measurements on $\text{La}_4\text{Ni}_3\text{O}_{10}$ single crystals provide consistent and reproducible results (Figs. S4-5), confirming intrinsic superconductivity under high pressure. To clarify the emergence of superconductivity, we perform *in situ* high pressure XRD measurements up to 80 GPa. As shown in Fig. S6, except for two peaks arising from the Re gasket, all peaks could be indexed well to $\text{La}_4\text{Ni}_3\text{O}_{10}$ with the monoclinic structure. With the pressure increasing, both the lattice parameters and unit cell volume decrease continuously (Fig. 3e, Fig. S6). At around 12 GPa, the (0 2 0) and (2 0 -1) peaks merge into one peak, suggesting the occurrence of structural phase transition (Fig. 3c). The structural analysis revealed that *in situ* high pressure XRD patterns above 12 GPa can be well described with the tetragonal $I4/mmm$ space group (No. 139). The enthalpy difference relative to $I4/mmm$ phase within 20 GPa is plotted in Fig. 3(d). From 0 GPa to 15 GPa [inset of Fig. 3(d)], we optimized the ions' positions, cell shape, and cell volume, and the enthalpy difference between the $P2_1/a$ phase and $I4/mmm$ phase decreases with pressure. When pressure is higher than 15 GPa, the $P2_1/a$ phase transforms to $I4/mmm$ phase after structural optimization owing to the sensitivity of the NiO_6 octahedra stacking angles. Hence, we compress the volume with the ions' positions and volume shape fixed based on the optimized $P2_1/a$ structure at 15 GPa for the enthalpy calculations above 15 GPa. The enthalpy of $P2_1/a$ phase is higher than that of $I4/mmm$ phase after 15.2 GPa, illustrating that $I4/mmm$ phase is more energetically stable than $P2_1/a$ phase under high pressure, which is in agreement with *in situ* high pressure XRD measurements. Accompany by the phase transition, the Ni-O-Ni angles change from 165.1° to 180° within a layer, which leads to the buckled Ni-O planes become flatten (Inset of Fig. 3d). Similar to cuprates, the appearance of quasi-two-dimensional structure under pressure paves the way for the emergence of high-temperature superconductivity in nicklates.

Based on the above high-pressure characterizations, we construct the temperature-pressure phase diagram of $\text{La}_4\text{Ni}_3\text{O}_{10}$ as shown in Fig. 4a. In lower pressure region, the $\text{La}_4\text{Ni}_3\text{O}_{10}$ single crystal exhibits metal-to-metal transition with a density-wave resistance anomaly. As the pressure increases, the resistance anomaly is gradually

suppressed. Upon further increasing pressure, superconductivity appears between 10-20 GPa, and the superconducting transition temperature T_c reaches 25 K over 50 GPa. In addition, concomitant with the enhancement of superconductivity in this pressure range, the strange metal behavior becomes gradually evident above 30 GPa. As can be seen from the phase diagram, the competition between resistance anomaly and superconductivity resembles the situation in some charge or spin density wave materials. All these observations indicate that high-temperature superconductivity can also be achieved in the pressurized $\text{La}_4\text{Ni}_3\text{O}_{10}$ single crystals.

Theoretical analysis. The pairing in pressurized $\text{La}_4\text{Ni}_3\text{O}_{10}$ is induced by the AFM super-exchange interaction under the strong Hubbard repulsion. As shown in Fig. 4b, each unit cell contains three Ni- atoms located on three different layers, with each Ni-atom hosting two 3d orbitals, i.e. the $3d_{z^2}$ and $3d_{x^2-y^2}$. The $3d_{z^2}$ orbital hosts a large interlayer hopping t_{\perp}^z , inducing a strong AFM interlayer super-exchange J_{\perp}^z ; while the $3d_{x^2-y^2}$ orbital hosts a relatively smaller intralayer hopping t_{\parallel}^x , inducing a weaker intralayer super-exchange J_{\parallel}^x . In addition, Hund's rule aligns spins in two orbitals on the same site. Hence, it transfers the nearest-neighbor super-exchange interaction from one orbital to the other³⁶, as shown in Fig. 4c, but with considerably reduced averaged strength because the transfer only takes place when the two orbitals on the same site are both singly occupied, while in the realistic Ni-3d^{7,33} configuration, they have only 2/3 possibility to be singly-occupied²¹. Similar to the cuprates, these super-exchange interactions can serve as effective pairing interactions in pressurized $\text{La}_4\text{Ni}_3\text{O}_{10}$. While both orbitals are near 1/3-filling²¹, the $3d_{z^2}$ orbital dominates the pairing because its weak intralayer hopping enhances the density of state.

The lower T_c in pressurized $\text{La}_4\text{Ni}_3\text{O}_{10}$ than that in pressurized $\text{La}_3\text{Ni}_2\text{O}_7$ originates from the pairing frustration effect caused by its trilayer structure. In bilayer $\text{La}_3\text{Ni}_2\text{O}_7$, driven by the interlayer super-exchange interaction, the pairing is mainly between the two layers^{33, 34, 36}, experiencing no frustration. However, in trilayer $\text{La}_4\text{Ni}_3\text{O}_{10}$, as shown in Fig. 4d, when an inner-layer $3d_{z^2}$ electron pairs with an upper outer-layer $3d_{z^2}$

electron driven by J_{\perp}^z , the lower outer-layer $3d_{z^2}$ electron is left single. That electron has to seek to pair with neighboring electrons within the same layer. Since the intralayer super-exchange interaction J_{\parallel}^z for $3d_{z^2}$ electron is weak, such a pairing is fragile and easily destroyed by thermal fluctuation. This pairing frustration effect in pressurized $\text{La}_4\text{Ni}_3\text{O}_{10}$ leads to a much lower T_c than that in pressurized $\text{La}_3\text{Ni}_2\text{O}_7$.

Conclusion

We have successfully grown high-quality single crystals of $\text{La}_4\text{Ni}_3\text{O}_{10}$ and performed a series of transport measurements both at ambient pressure and high pressure. We found pressure-induced superconductivity with a T_c at approximately 25 K. The emergence of superconductivity accompanied by the phase transition from $P2_1/a$ to $I4/mmm$, leads to the buckled Ni-O planes become flatten ultimately. Theoretical analysis displays the AFM super-exchange interactions can serve as the effective pairing interaction for the emergence of superconductivity in pressurized $\text{La}_4\text{Ni}_3\text{O}_{10}$ single crystals. Our results demonstrate that high-temperature superconductivity can be achieved in other members of RP phases, from which we can explore the unconventional superconductivity in nickelates.

Note added: After we submitted to preprint (arXiv: 2311.07423), we became aware that there was another paper by Zhu et al. (arXiv:2311.07353) posted on arXiv on the same day⁴⁷. They reported resistance measurements on $\text{La}_4\text{Ni}_3\text{O}_{10}$ single crystals, which is consistent with our data.

Methods

Material synthesis and characterization

Single crystals of $\text{La}_4\text{Ni}_3\text{O}_{10}$ were grown by the high-pressure optical floating zone technique. Raw materials of La_2O_3 (99.99%) were dried at 900 °C overnight before the reaction, and then mixed with an appropriate amount of NiO. The mixture was ground thoroughly, pressed into pellets, and sintered at 1200 °C for 2 days with several intermediate grindings. The powders were pressed into seed and feed rods with a diameter of about 6 mm and sintered at 1300 °C for 2 hours. Subsequent single crystal growth was performed in a high-pressure optical floating zone furnace (HKZ-300) with a growth rate of 5 mm/h and 20 bar of oxygen. Single crystals larger than 5 mm in size can be obtained. The Powder X-ray diffraction (PXRD) patterns were taken using a Bruker D2 phaser with Cu-K_α radiation ($\lambda = 1.5418 \text{ \AA}$) at room temperature. Energy-dispersive X-ray spectroscopy (EDS) was employed to determine the compositions of single crystals. X-ray Photoelectron. The high-resolution scanning transmission electron microscopy (TEM) imaging was taken in JEM-ARM300F GRAND ARM.

STM measurements

$\text{La}_4\text{Ni}_3\text{O}_{10}$ single crystals were cleaved at 77 K with a background pressure of 2×10^{-10} Torr and then were immediately transferred into the STM head for measurements. STM experiments were performed within a Unisoku low-temperature STM. All of the STM data were obtained at 4.3 K.

ARPES measurements

High-resolution angle-resolved photoemission spectroscopy (ARPES) experiments were conducted at beamline 03U in Shanghai Synchrotron Radiation Facility (SSRF). The samples were cleaved in situ under ultra-high vacuum below 7×10^{-11} mbar. Data were collected with a Scienta DA30 electron analyser. The total energy and angular resolutions were set to 20 meV and 0.2° , respectively.

First-principles calculations

First-principles band structure calculations were performed using Vienna ab initio simulation package (VASP)^{48,49} with a plane wave basis. Band structure: The exchange-correlation energy was considered under Perdew-Burke-Ernzerhof (PBE) type generalized gradient approximation (GGA)⁵⁰ with spin-orbit coupling included. Hubbard $U = 4.0$ eV was applied to describe the localized 3d orbitals of Ni atoms. The cutoff energy for the plane-wave basis was set to 400 eV. A Γ -centered Monkhorst-Pack k-point mesh of $19 \times 19 \times 5$ was adopted in the self-consistent calculations. The enthalpy difference calculation: The calculations use projector-augmented wave (PAW)⁵¹ approach to describe the core electrons and their effects on valence orbitals and consider the $5s^2 5p^6 5d_1 6s_2$ for La, $3d^8 4s^2$ for Ni and $2s^2 2p^4$ for O. We set the plane-wave kinetic-energy cutoff to 700 eV, and the Brillouin zone is sampled with the special k-mesh generated by the Monkhorst-Pack scheme with a k-point spacing of $2\pi \times 0.025 \text{ \AA}^{-1}$. The convergence tolerance is 10^{-6} eV for total energy and all forces are converged to be less than 0.003 eV/\AA . At ambient pressure, the calculated volume is less than 1% larger than the experimental data, suggesting the reliability of the calculation.

Transport properties under ambient and high pressure

Resistivity, heat capacity, and magnetic susceptibility under ambient pressure were measured using the Physical Property Measurement System (Dynacool, Quantum Design) and SQUID vibrating sample magnetometer (MPMS3, Quantum Design). High-pressure electrical transport measurements were performed in a diamond anvil cell (DAC) with culets of 200 μm and 300 μm . The cubic BN/epoxy mixture was used as an insulator layer between the BeCu gasket and electrical leads. Four Pt foils were arranged according to the van der Pauw method^{52, 53}. We use NaCl as a pressure-transmitting medium (PTM) to improve the hydrostatic environment. *In situ* high pressure XRD measurements were performed at the beamline 15U in the Shanghai Synchrotron Radiation Facility ($\lambda=0.6199 \text{ \AA}$) and Mineral oil was used as PTM. The pressure was determined by the ruby luminescence method⁵⁴.

Acknowledgment

We are grateful for the stimulating discussions with Chen Lu and Zhiming Pan. This work was supported by the National Natural Science Foundation of China (Grant No. 52272265), the National Key R&D Program of China (Grant Nos. 2023YFA1607400 and 2018YFA0704300). L.X.Y. acknowledges the financial support from the National Key R&D Program of China (Grants No. 2022YFA1403200 and 2022YFA1403100) and the National Natural Science Foundation of China (Grant No. 12275148). S.C.Y. acknowledges the financial support from the National Key R&D program of China (2020YFA0309602, 2022YFA1402703). F.Y. acknowledges the financial support from the National Natural Science Foundation of China (Grant No. 12074031). H.J.G acknowledges the financial support from the National Natural Science Foundation of China (Grant No. 12004270) and Guangdong Basic and Applied Basic Research Foundation (Grant No. 2022B1515120020). C.J.W. is supported by the National Natural Science Foundation of China (Grants No. 12234016 and 12174317) and the New Cornerstone Science Foundation. The authors thank the Analytical Instrumentation Center (# SPST-AIC10112914), SPST, ShanghaiTech University. The authors thank the staff from BL15U1 at Shanghai Synchrotron Radiation Facility for assistance during data collection.

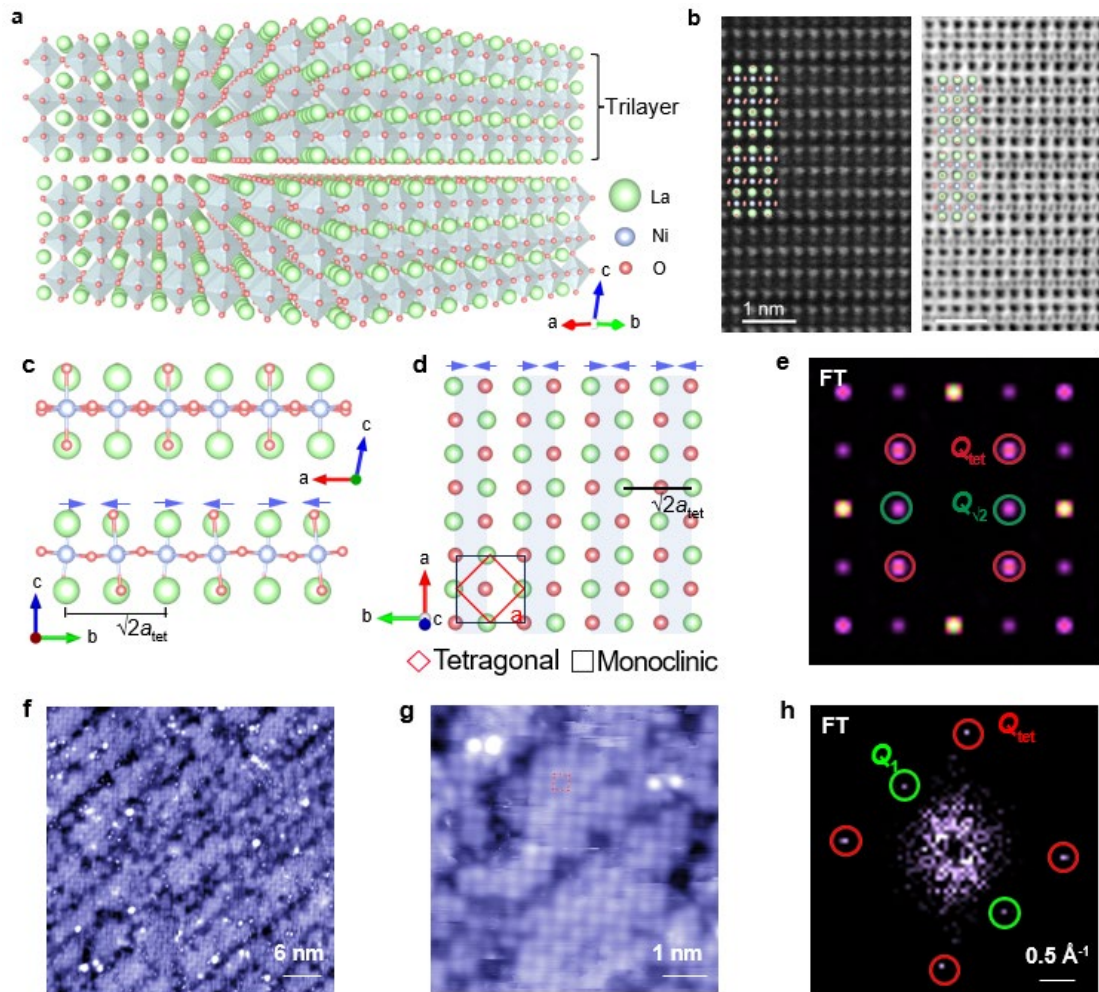


Fig.1|Crystal structure and surface topographies of $\text{La}_4\text{Ni}_3\text{O}_{10}$ single crystals. **a**, schematic illustration of the crystal structure of $\text{La}_4\text{Ni}_3\text{O}_{10}$ crystal. **b**, high-angle annular dark-field (left) and annular bright-field (right) STEM images of $\text{La}_4\text{Ni}_3\text{O}_{10}$ along the b axis. **c**, side-view crystal structures along the ac plane (upper) and the bc plane (lower), respectively. **d**, the top-view crystal structure of the LaO surface. The appended red and black squares are the unit cells for the tetragonal and monoclinic phases. The light blue ribbons indicate the unidirectional reconstruction. **e**, FT image of the schematic crystal structure shown in **d**. The red and green circles indicate the tetragonal Bragg lattice (Q_{tet}) and the unidirectional structural distortion pattern ($Q_{1/2}$), respectively. **f**, **g**, Constant-current STM topographies taken on the LaO surface. **h**, FT image of the STM topography shown in **g**.

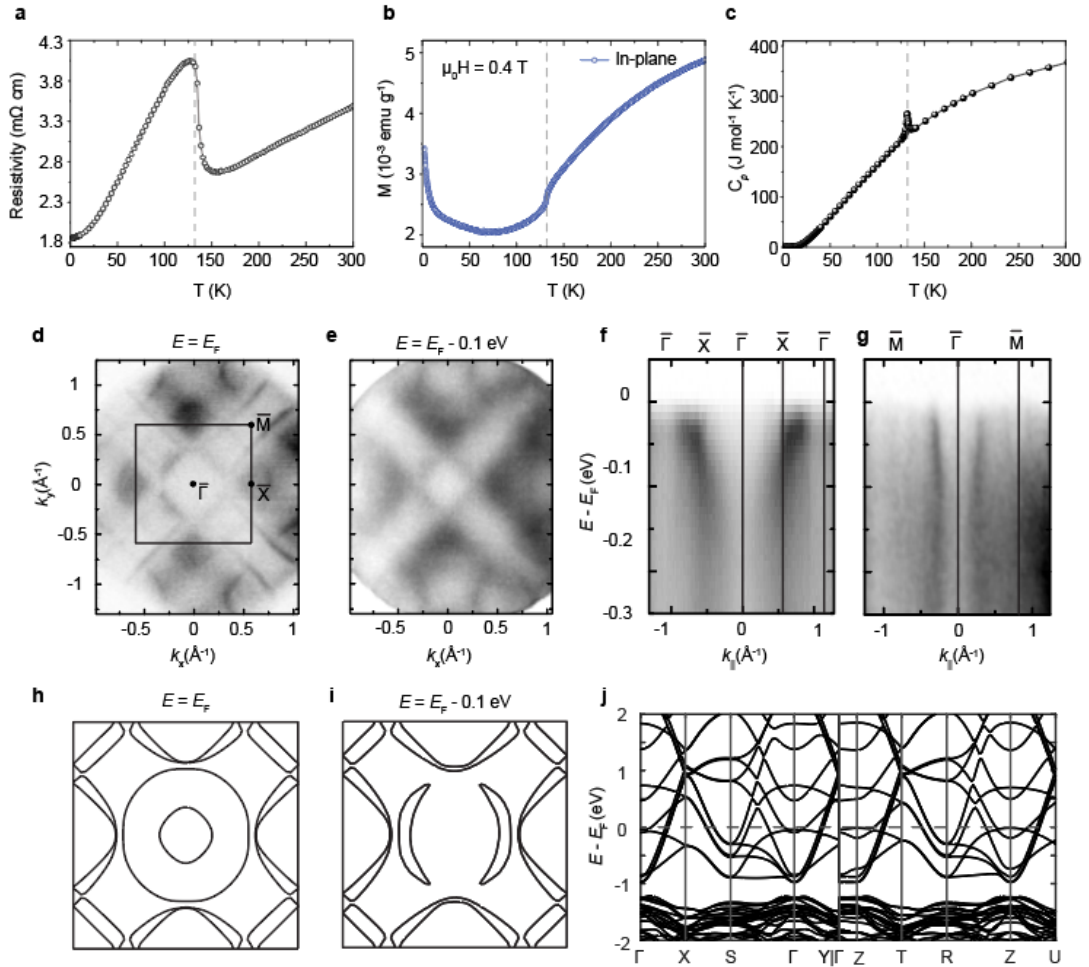


Fig.2|Physical properties and electronic structure of $\text{La}_4\text{Ni}_3\text{O}_{10}$ single crystals. **a**, temperature-dependent resistivity. **b**, temperature-dependent magnetic susceptibility. **c**, temperature-dependent heat capacity. **d**, **e**, experimental constant energy contours measured by ARPES at selected energies, with surface Brillouin zone indicated by the black rectangle. **f**, **g**, experimental band dispersions along the $\bar{\Gamma}\bar{X}$ and $\bar{\Gamma}\bar{M}$ directions, respectively. Data were collected using linear-horizontally (LH) polarized photons at 74 eV at 18 K. **h**, **i**, calculated constant energy contours at selected energies. **j**, calculated band structure along high-symmetry directions. The dashed line indicates the Fermi level.

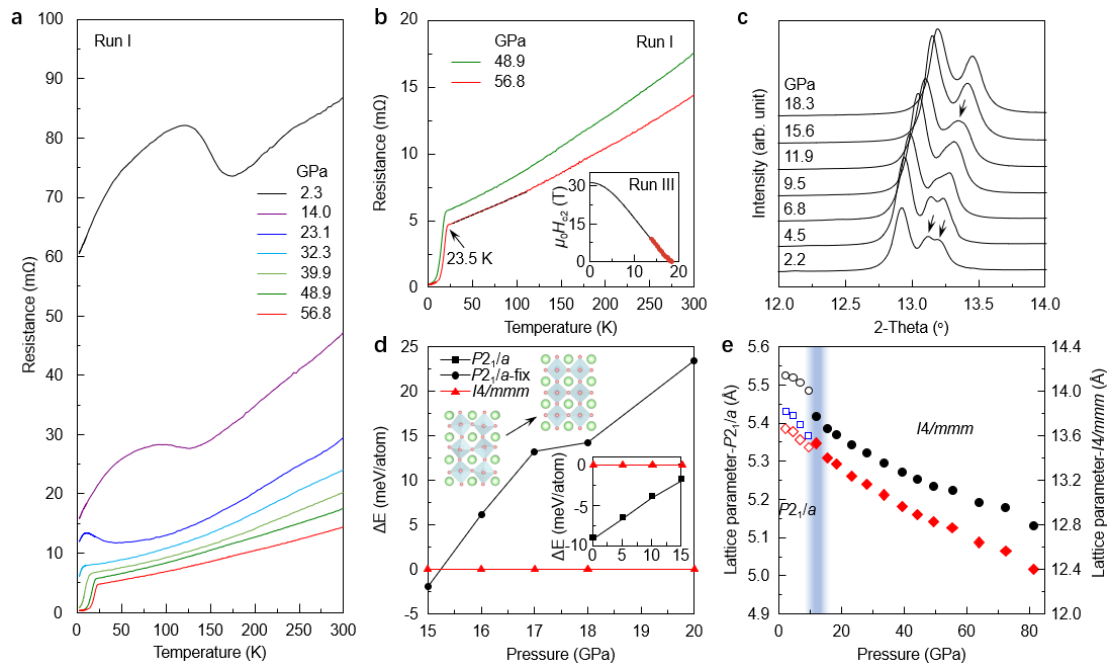


Fig.3|Transport properties of $\text{La}_4\text{Ni}_3\text{O}_{10}$ single crystals as a function of pressure. a, electrical resistance of $\text{La}_4\text{Ni}_3\text{O}_{10}$ as a function of temperature from 2.3 GPa to 56.8 GPa in Run 1. **b,** linear resistance in the normal state. The inset shows the temperature dependence of the upper critical field for $\text{La}_4\text{Ni}_3\text{O}_{10}$ at 67.7 GPa in Run 3. T_c is determined as the 90% of the resistance at the onset T_c . The solid lines represent the Ginzburg-Landau (G-L) fitting. **c,** the circles represent the difference in enthalpy between the space groups $P2_1/a$ and $I4/mmm$ as a function of pressure calculated using the first-principles method. The inset shows the modification of NiO_6 octahedra stacking mode under pressure. **d,** synchrotron XRD patterns of powder samples. Details of the evolutions of the (0 2 0) and (2 0 -1) peaks under pressure. **e,** the evolution of lattice parameters refined from the XRD patterns.

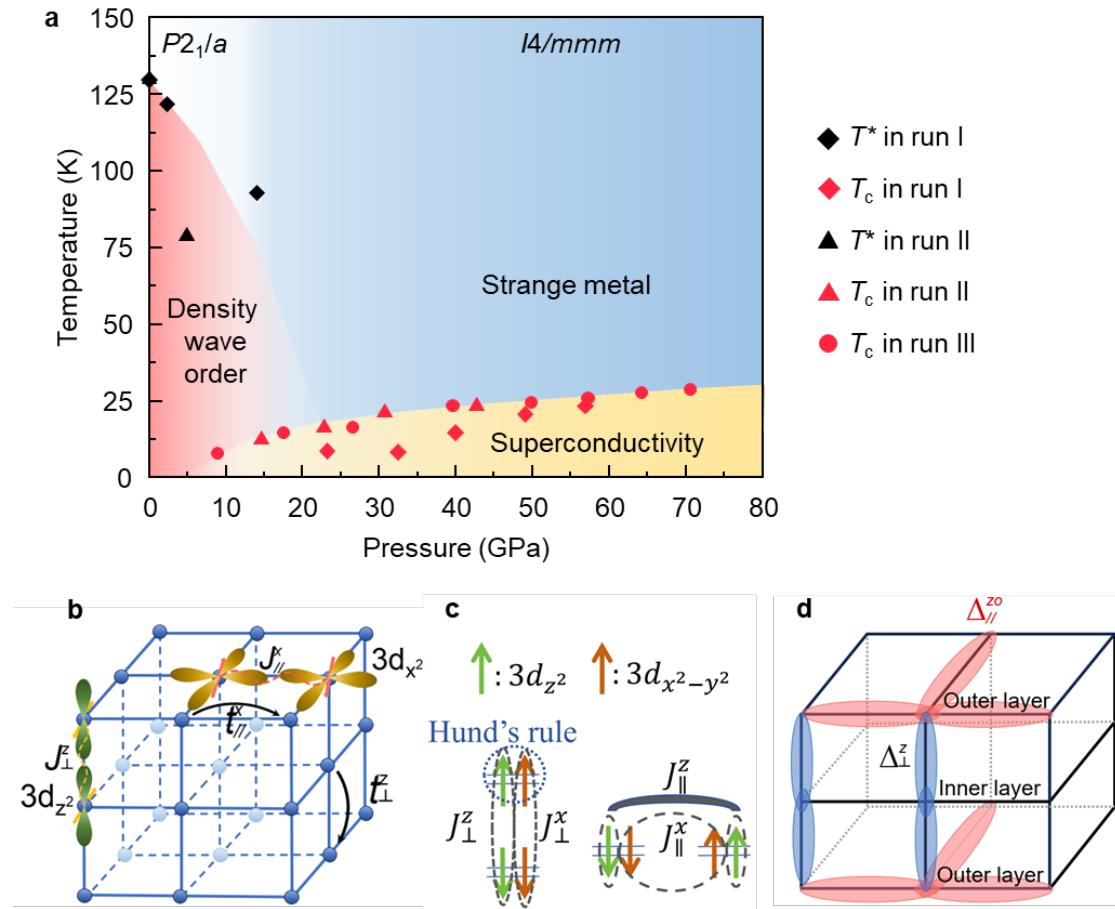


Fig.4| The phase diagram and theoretical model of pressurized $\text{La}_4\text{Ni}_3\text{O}_{10}$. **a**, phase diagram under pressure. The yellow symbols represent the density-wave (DW) transition T^* measured at various pressures. The red symbols represent the superconducting transition temperatures T_c determined from the various runs. **b**, the relevant orbitals, their couplings, and direct super-exchange interactions J_{\perp}^z and J_{\parallel}^x . **c**, an illustration of the effective super-exchange interactions transferred from one orbital to the other induced by Hund's rule coupling. Note that such transfer only takes place when both orbitals are singly occupied, while in the realistic Ni-3d^{7.33} configuration, these orbitals have only a 2/3 possibility of being singly occupied. **d**, the dominant superconducting pairings.

Reference

1. Bednorz JG, Müller KA. Possible highTc superconductivity in the Ba–La–Cu–O system. *Zeitschrift für Physik B Condensed Matter* 1986, **64**(2): 189-193.
2. Takagi H, Eisaki H, Uchida S, Maeda A, Tajima S, Uchinokura K, *et al.* Transport and optical studies of single crystals of the 80-K Bi–Sr–Ca–Cu–O superconductor. *Nature* 1988, **332**(6161): 236-238.
3. Keimer B, Kivelson SA, Norman MR, Uchida S, Zaanen J. From quantum matter to high-temperature superconductivity in copper oxides. *Nature* 2015, **518**(7538): 179-186.
4. Lee PA, Nagaosa N, Wen X-G. Doping a Mott insulator: Physics of high-temperature superconductivity. *Reviews of Modern Physics* 2006, **78**(1): 17-85.
5. Kamihara Y, Watanabe T, Hirano M, Hosono H. Iron-Based Layered Superconductor La[O_{1-x}F_x]FeAs (x = 0.05–0.12) with T_c = 26 K. *Journal of the American Chemical Society* 2008, **130**(11): 3296-3297.
6. Wen H-H, Mu G, Fang L, Yang H, Zhu X. Superconductivity at 25 K in hole-doped (La_{1-x}Sr_x)OFeAs. *Europhysics Letters* 2008, **82**(1): 17009.
7. Platt C, Hanke W, Thomale R. Functional renormalization group for multi-orbital Fermi surface instabilities. *Advances in Physics* 2013, **62**(4-6): 453-562.
8. Yi M, Zhang Y, Shen Z-X, Lu D. Role of the orbital degree of freedom in iron-based superconductors. *npj Quantum Materials* 2017, **2**(1): 57.
9. Anisimov VI, Bukhvalov D, Rice TM. Electronic structure of possible nickelate analogs to the cuprates. *Physical Review B* 1999, **59**(12): 7901-7906.
10. Li D, Lee K, Wang BY, Osada M, Crossley S, Lee HR, *et al.* Superconductivity in an infinite-layer nickelate. *Nature* 2019, **572**(7771): 624-627.
11. Li D, Wang BY, Lee K, Harvey SP, Osada M, Goodge BH, *et al.* Superconducting Dome in Nd_{1-x}Sr_xNiO₂ Infinite Layer Films. *Physical Review Letters* 2020, **125**(2): 027001.
12. Osada M, Wang BY, Goodge BH, Harvey SP, Lee K, Li D, *et al.* Nickelate Superconductivity without Rare-Earth Magnetism: (La,Sr)NiO₂. *Advanced Materials* 2021, **33**(45): 2104083.
13. Osada M, Wang BY, Goodge BH, Lee K, Yoon H, Sakuma K, *et al.* A Superconducting Praseodymium Nickelate with Infinite Layer Structure. *Nano Letters* 2020, **20**(8): 5735-5740.

14. Pan GA, Ferenc Segedin D, LaBollita H, Song Q, Nica EM, Goodge BH, *et al.* Superconductivity in a quintuple-layer square-planar nickelate. *Nature Materials* 2022, **21**(2): 160-164.
15. Wang NN, Yang MW, Yang Z, Chen KY, Zhang H, Zhang QH, *et al.* Pressure-induced monotonic enhancement of T_c to over 30 K in superconducting $\text{Pr}_{0.82}\text{Sr}_{0.18}\text{NiO}_2$ thin films. *Nature Communications* 2022, **13**(1): 4367.
16. Sun H, Huo M, Hu X, Li J, Liu Z, Han Y, *et al.* Signatures of superconductivity near 80 K in a nickelate under high pressure. *Nature* 2023, **621**(7979): 493-498.
17. Hou J, Yang PT, Liu ZY, Li JY, Shan PF, Ma L, *et al.* Emergence of High-Temperature Superconducting Phase in Pressurized $\text{La}_3\text{Ni}_2\text{O}_7$ Crystals. *Chinese Physics Letters* 2023, **40**(11): 117302.
18. Zhang Y, Su D, Huang Y, Sun H, Huo M, Shan Z, *et al.* High-temperature superconductivity with zero-resistance and strange metal behavior in $\text{La}_3\text{Ni}_2\text{O}_7$. 2023. p. arXiv:2307.14819.
19. Zhang M, Pei C, Wang Q, Zhao Y, Li C, Cao W, *et al.* Effects of pressure and doping on Ruddlesden-Popper phases $\text{La}_{n+1}\text{Ni}_n\text{O}_{3n+1}$. *Journal of Materials Science & Technology* 2024, **185**: 147-154.
20. Wang G, Wang N, Hou J, Ma L, Shi L, Ren Z, *et al.* Pressure-induced superconductivity in polycrystalline $\text{La}_3\text{Ni}_2\text{O}_7$. 2023. p. arXiv:2309.17378.
21. Sakakibara H, Ochi M, Nagata H, Ueki Y, Sakurai H, Matsumoto R, *et al.* Theoretical analysis on the possibility of superconductivity in a trilayer Ruddlesden-Popper nickelate $\text{La}_4\text{Ni}_3\text{O}_{10}$ under pressure and its experimental examination: comparison with $\text{La}_3\text{Ni}_2\text{O}_7$. 2023. p. arXiv:2309.09462.
22. Li Q, Zhang Y-J, Xiang Z-N, Zhang Y, Zhu X, Wen H-H. Signature of Superconductivity in Pressurized $\text{La}_4\text{Ni}_3\text{O}_{10}$. *Chinese Physics Letters* 2024, **41**(1): 017401.
23. Liu Z, Huo M, Li J, Li Q, Liu Y, Dai Y, *et al.* Electronic correlations and energy gap in the bilayer nickelate $\text{La}_3\text{Ni}_2\text{O}_7$. 2023. p. arXiv:2307.02950.
24. Luo Z, Hu X, Wang M, Wú W, Yao D-X. Bilayer Two-Orbital Model of $\text{La}_3\text{Ni}_2\text{O}_7$ under Pressure. *Physical Review Letters* 2023, **131**(12): 126001.
25. Luo Z, Lv B, Wang M, Wú W, Yao D-x. High- T_c superconductivity in $\text{La}_3\text{Ni}_2\text{O}_7$ based on the bilayer two-orbital t-J model. 2023. p. arXiv:2308.16564.
26. Shen Y, Qin M, Zhang G-M. Effective Bi-Layer Model Hamiltonian and Density-Matrix Renormalization Group Study for the High- T_c Superconductivity in $\text{La}_3\text{Ni}_2\text{O}_7$ under High Pressure. *Chinese Physics Letters* 2023, **40**(12): 127401.
27. Yang Y-f, Zhang G-M, Zhang F-C. Interlayer valence bonds and two-component theory for high- T_c superconductivity of $\text{La}_3\text{Ni}_2\text{O}_7$ under pressure. *Physical Review B* 2023, **108**(20): L201108.

28. Zhang Y, Lin L-F, Moreo A, Dagotto E. Electronic structure, dimer physics, orbital-selective behavior, and magnetic tendencies in the bilayer nickelate superconductor $\text{La}_3\text{Ni}_2\text{O}_7$ under pressure. *Physical Review B* 2023, **108**(18): L180510.
29. Zhang Y, Lin L-F, Moreo A, Maier TA, Dagotto E. Trends in electronic structures and S_{\pm} -wave pairing for the rare-earth series in bilayer nickelate superconductor $\text{R}_3\text{Ni}_2\text{O}_7$. *Physical Review B* 2023, **108**(16): 165141.
30. Yang J, Sun H, Hu X, Xie Y, Miao T, Luo H, *et al.* Orbital-Dependent Electron Correlation in Double-Layer Nickelate $\text{La}_3\text{Ni}_2\text{O}_7$. 2023. p. arXiv:2309.01148.
31. Yang Q-G, Wang D, Wang Q-H. Possible S_{+-} -wave superconductivity in $\text{La}_3\text{Ni}_2\text{O}_7$ *Physical Review B* 2023, **108**(14): L140505.
32. Sakakibara H, Kitamine N, Ochi M, Kuroki K. Possible high T_c superconductivity in $\text{La}_3\text{Ni}_2\text{O}_7$ under high pressure through manifestation of a nearly-half-filled bilayer Hubbard model. 2023. p. arXiv:2306.06039.
33. Lu C, Pan Z, Yang F, Wu C. Interplay of two E_g orbitals in Superconducting $\text{La}_3\text{Ni}_2\text{O}_7$ Under Pressure. 2023. p. arXiv:2310.02915.
34. Pan Z, Lu C, Yang F, Wu C. Effect of Rare-earth Element Substitution in Superconducting $\text{R}_3\text{Ni}_2\text{O}_7$ Under Pressure. 2023. p. arXiv:2309.06173.
35. Nakata M, Ogura D, Usui H, Kuroki K. Finite-energy spin fluctuations as a pairing glue in systems with coexisting electron and hole bands. *Physical Review B* 2017, **95**(21): 214509.
36. Lu C, Pan Z, Yang F, Wu C. Interlayer Coupling Driven High-Temperature Superconductivity in $\text{La}_3\text{Ni}_2\text{O}_7$ Under Pressure. 2023. p. arXiv:2307.14965.
37. Lechermann F, Gondolf J, Bötzel S, Eremin IM. Electronic correlations and superconducting instability in $\text{La}_3\text{Ni}_2\text{O}_7$ under high pressure. *Physical Review B* 2023, **108**(20): L201121.
38. Liu Y-B, Mei J-W, Ye F, Chen W-Q, Yang F. S_{+-} -Wave Pairing and the Destructive Role of Apical-Oxygen Deficiencies in $\text{La}_3\text{Ni}_2\text{O}_7$ under Pressure. *Physical Review Letters* 2023, **131**(23): 236002.
39. Gu Y, Le C, Yang Z, Wu X, Hu J. Effective model and pairing tendency in bilayer Ni-based superconductor $\text{La}_3\text{Ni}_2\text{O}_7$. 2023. p. arXiv:2306.07275.
40. Zhang J, Zheng H, Chen Y-S, Ren Y, Yonemura M, Huq A, *et al.* High oxygen pressure floating zone growth and crystal structure of the metallic nickelates $\text{R}_4\text{Ni}_3\text{O}_{10}$ (R=La,Pr). *Physical Review Materials* 2020, **4**(8): 083402.
41. Zhang J, Phelan D, Botana AS, Chen Y-S, Zheng H, Krogstad M, *et al.* Intertwined density waves in a metallic nickelate. *Nature Communications* 2020, **11**(1): 6003.

42. Zhang J, Botana AS, Freeland JW, Phelan D, Zheng H, Pardo V, *et al.* Large orbital polarization in a metallic square-planar nickelate. *Nature Physics* 2017, **13**(9): 864-869.
43. Shen Y, Sears J, Fabbris G, Li J, Pelliciani J, Jarrige I, *et al.* Role of Oxygen States in the Low Valence Nickelate $\text{La}_4\text{Ni}_3\text{O}_8$. *Physical Review X* 2022, **12**(1): 011055.
44. Greenblatt M. Molybdenum oxide bronzes with quasi-low-dimensional properties. *Chemical Reviews* 1988, **88**(1): 31-53.
45. Ortiz BR, Teicher SML, Hu Y, Zuo JL, Sarte PM, Schueller EC, *et al.* CsV_3Sb_5 : A Z_2 Topological Kagome Metal with a Superconducting Ground State. *Physical Review Letters* 2020, **125**(24): 247002.
46. Li H, Zhou X, Nummy T, Zhang J, Pardo V, Pickett WE, *et al.* Fermiology and electron dynamics of trilayer nickelate $\text{La}_4\text{Ni}_3\text{O}_{10}$. *Nature Communications* 2017, **8**(1): 704.
47. Zhu Y, Zhang E, Pan B, Chen X, Peng D, Chen L, *et al.* Superconductivity in trilayer nickelate $\text{La}_4\text{Ni}_3\text{O}_{10}$ single crystals. 2023. p. arXiv:2311.07353.
48. Kresse G, Furthmüller J. Efficient iterative schemes for ab initio total-energy calculations using a plane-wave basis set. *Physical Review B* 1996, **54**(16): 11169-11186.
49. Monkhorst HJ, Pack JD. Special points for Brillouin-zone integrations. *Physical Review B* 1976, **13**(12): 5188-5192.
50. Perdew JP, Burke K, Ernzerhof M. Generalized Gradient Approximation Made Simple. *Physical Review Letters* 1996, **77**(18): 3865-3868.
51. Blöchl PE. Projector augmented-wave method. *Physical Review B* 1994, **50**(24): 17953-17979.
52. Pei C, Ying T, Zhao Y, Gao L, Cao W, Li C, *et al.* Pressure-induced reemergence of superconductivity in BaIr_2Ge_7 and $\text{Ba}_3\text{Ir}_4\text{Ge}_{16}$ with cage structures. *Matter and Radiation at Extremes* 2022, **7**(3).
53. Pei C, Zhang J, Wang Q, Zhao Y, Gao L, Gong C, *et al.* Pressure-induced superconductivity at 32 K in MoB_2 . *National Science Review* 2023, **10**(5).
54. Mao HK, Xu J, Bell PM. Calibration of the ruby pressure gauge to 800 kbar under quasi-hydrostatic conditions. *Journal of Geophysical Research: Solid Earth* 1986, **91**(B5): 4673-4676.